Fragment Molecular Orbital Study on Electron Tunneling Mechanisms in Bacterial Photosynthetic Reaction Center

Hirotaka Kitoh-Nishioka* and Koji Ando

Department of Chemistry, Graduate School of Science, Kyoto University, Sakyo-ku, Kyoto 606-8502, Japan.

E-mail: nishioka@kuchem.kyoto-u.ac.jp

Phone: +81-75-753-4017. Fax: +81-75-753-4018

―――――――――――――――――――
*To whom correspondence should be addressed

Abstract

The tunneling mechanisms of electron transfers (ETs) in photosynthetic reaction center of *Blastochloris viridis* are studied by the *ab initio* fragment molecular orbital (FMO) method combined with the generalized Mulliken-Hush (GMH) and the bridge Green function (GF) calculations of the electronic coupling T_{DA} and the tunneling current method for the ET pathway analysis at the fragment-based resolution. For the ET from batctriopheophytin (H_L) to menaquinone (MQ), a major tunneling current through Trp M250 and a minor back flow via Ala M215, Ala M216, and His M217 are quantified. For the ET from MQ to ubiquinone, the major tunneling pathway via the non-heme Fe^{2+} and His L190 is identified as well as minor pathway via His M217 and small back flows involving His L230, Glu M232, and His M264. At the given molecular structure from X-ray experiment, the spin state of the Fe^{2+} ion, its replacement by Zn^{2+}, or its removal are found to affect the T_{DA} value by factors within 2.2. The calculated T_{DA} values, together with experimentally estimated values of the driving force and the reorganization energy, give the ET rates in reasonable agreement with experiments.

Keywords: electron transfer, electronic coupling, pathway analysis, *ab initio*, FMO-LCMO, non-heme iron

INTRODUCTION

A useful theoretical framework for biological electron transfer (ET) rates is the semi-classical Marcus formula[1]

$$k_{\mathrm{DA}} = \frac{2\pi}{\hbar} \frac{|T_{\mathrm{DA}}|^2}{\sqrt{4\pi\lambda k_{\mathrm{B}}T}} \exp\left[-\frac{(-\Delta G - \lambda)^2}{4\lambda k_{\mathrm{B}}T}\right], \tag{1}$$

where T_{DA} is the electronic coupling, $-\Delta G$ is the reaction driving force, λ is the reorganization energy, T is the temperature, k_{B} is the Boltzmann constant, and $\hbar$ is the Planck constant divided by 2π. The chemical and structural arrangements of the redox centers and the protein environment are considered to regulate the ET rate by adjusting the parameters, T_{DA}, $-\Delta G$, and λ, toward efficient and controlled energy conversions in photosynthesis and respiration. Experimental studies have shown that such biological ETs occur via long-distance single-electron tunneling between redox centers separated by 5 - 30 Å,[2–6] in which the protein environment provides intermediate virtual states for super-exchange electronic coupling[7] in T_{DA}, and thereby the protein's secondary and tertiary structures remarkably affect the ET rate.[4–6] However, it is generally difficult to separate the reorganization part λ and the electronic part T_{DA} from the observed ET rate, which causes uncertainties in their experimental evaluation. It is furthermore a formidable challenge to resolve the parts of the protein that are most significantly contributing to the ET tunneling pathways. Theoretical studies of T_{DA} calculation and tunneling pathway analysis are therefore of fundamental importance for understanding the mechanism of biological ET reactions.

So far, various theoretical methods have been developed, including the *Pathways* model,[8] the path integral method,[9] packing density model,[10,11] tube model,[12] artificial intelligence method,[13] ET contact map,[14] tunneling current method,[15–20] worm model,[21] averaged tunneling routes corrected by the quantum-interference effect[22] (for reviews, see Refs. 23–25). Many of these employed the extended Hückel[12,13,15,19–22] or semi-empirical molecular-orbital (MO) calculations[14,18] when applied to large protein systems. On the other hand, *ab initio* quantum mechanical (QM) studies have been mostly limited to ET and excitation energy

transfers in small organic molecules, at levels ranging from the Hartree-Fock (HF)[26–28] to the configuration interaction (CI)-singles[29,30] and multi-configuration self-consistent field (MC-SCF) methods.[31] Despite these developments, application of the *ab initio* QM methods to realistic biological ET proteins has been hindered by the huge computational cost. Thus, model systems with simplified amino-acid structures or the *pruned* models of up to a few hundred atoms have been examined previously.[16,32–38] Compared to these T_{DA} calculations, the tunneling-pathway analysis of such model/pruned systems at *ab initio* QM level is rather scarce.[38,39]

To the *ab initio* QM calculations of large systems, the fragment molecular orbital (FMO) method[40–42] is an effective and practical approach. It divides the total system into fragments and the electronic structure of each fragment is determined self-consistently under the Coulomb field of all other fragment monomers. The calculation on each fragment dimer is then performed under the Coulomb field of all other fragment monomers.[40–42] The method has been successfully applied to large protein systems.[43–45] Nonetheless, its original form is not designed for calculating the electronic wave function of the total system. This problem has been addressed recently by the method of FMO-LCMO (linear combination of molecular orbitals) by Tsuneyuki et al.[46] It produces the Hamiltonian matrix and the canonical MOs of the whole system from the fragment monomer and dimer outputs of FMO calculations with small additional computational cost.[46]

On the basis of these developments, we recently proposed[47] an approach to studying long-distance ETs in large systems by combining the FMO-LCMO method with the bridge Green function (GF) and the tunneling current theories. It has been demonstrated to yield accurate T_{DA} values and provide an efficient way to analyze ET pathways at the fragment-based resolution. In particular, size reduction of the FMO-LCMO Hamiltonian to the valence-only space was found to be accurate and useful. This brings significant saving of computational cost when large basis sets were used.[48] However, the applications were limited to rather simple model systems with symmetric structure and/or homogeneous bridges. It is thus needed

4

to assess this approach to more realistic systems with non-symmetric and inhomogeneous structures.

In this work, we analyze the mechanism of ETs from bacteriopheophytin to primary quinone (Q_A) and then to secondary quinone (Q_B) in bacterial photosynthetic reaction center (RC). Previous theoretical studies on these ETs have applied square barrier models,[2,3,10] the extended Hückel,[20,22,49] semi-empirical MO,[50] and *ab initio* MO methods.[37,39] However, tunneling-pathway analysis at the *ab initio* QM level has been reported only in one paper[39] to our knowledge. In particular, the role of non-heme iron (Fe^{2+}) in the electron tunneling from Q_A to Q_B has been left unclear since the Fe^{2+} ion was either removed,[39] replaced by a zinc ion (Zn^{2+}),[37] or modeled by simple *p*-orbitals.[49] To address these problems, here we apply our approach[47] to the T_{DA} calculation and the tunneling pathway analysis. We also examine the generalized Mulliken-Hush (GMH)[51,52] method whose applicability to large and inhomogeneous biological ET systems has not been well-explored previously.

As a result, we find that the spin state of the Fe^{2+} ion, its replacement by Zn^{2+}, or its removal affects the T_{DA} by factors smaller than 2.2. They also yield the ET rates in reasonable agreement with experiments when combined with experimentally estimated values of the driving force and the reorganization energy. We also confirmed that both the GMH and the bridge GF methods reproduced reasonable T_{DA} values in comparison with the all-electron calculations of the non-fragmented systems. (Hereafter, such all-electron calculations for obtaining the reference T_{DA} values will be simply denoted by restricted HF (RHF) or unrestricted HF (UHF).) Finally, the electron tunneling pathway analysis has been carried out at the fragment-based resolution to identify the most contributing amino acids.

Theory

We begin with the FMO method with fragment dimer correction (FMO2) where the total electronic energy, E_{tot}, is approximated by[40,41]

$$E_{\text{tot}} = \sum_{I>J} E_{IJ} - (N-2) \sum_I E_I, \tag{2}$$

where N is the number of the fragment monomers, and E_I and E_{IJ} are the electronic energies of the fragment monomer I and the fragment dimer IJ, respectively.

The FMO-LCMO calculation utilizes the canonical MOs and orbital energies of all monomers and dimers from the FMO2 calculation.[46] By using these output data, one-electron Hamiltonian matrices of fragment monomers and dimers are constructed as

$$(H_I)_{I_p,I_q} = \epsilon_{I_p} \delta_{I_p,I_q}, \tag{3}$$

$$(H_{IJ})_{IJ_a,IJ_b} = \epsilon_{IJ_a} \delta_{IJ_a,IJ_b}. \tag{4}$$

where the subscripts I_p and IJ_a denote the p-th canonical MO of the fragment monomer I and the a-th canonical MO of the fragment dimer IJ, respectively. ϵ_{I_p} and ϵ_{IJ_a} are the corresponding MO energies. The one-electron Hamiltonian matrix of fragment dimers in the dimer MO representation is transformed to the monomer MO representation by

$$(H_{IJ})_{L_p,M_q} = \sum_{IJ_a} \epsilon_{IJ_a} \langle \phi_p^L | \phi_a^{IJ} \rangle \langle \phi_a^{IJ} | \phi_q^M \rangle, \tag{5}$$

where the $|\phi_p^L\rangle$ and $|\phi_a^{IJ}\rangle$ represent the canonical MOs L_p and IJ_a, respectively. Finally, the total one-electron Hamiltonian matrix in the monomer MO representation is approximated

by[46]

$$(H_{\text{total}})_{Ip,Jq} = (H_{IJ})_{Ip,Jq} \quad \text{for} \quad I \neq J, \tag{6}$$

$$(H_{\text{total}})_{Ip,Iq} = \sum_{J \neq I}(H_{IJ})_{Ip,Iq} - (N-2)(H_I)_{Ip,Iq}. \tag{7}$$

Here, the diagonal blocks, eq 7, have the same form as eq 2. The MOs and corresponding orbital energies of the total system is obtained by solving the generalized eigenvalues problem with the overlap matrix of monomer MOs.

In the FMO-LCMO scheme, limiting the number of monomer MOs expanding the matrices eqs 3 and 5 significantly reduces the size of total Hamiltonian matrix eqs 6 and 7[46] and thereby the computational cost for both constructing and diagonalizing it. In the previous report,[47] we limited the monomer MO space to the minimal valence space and found reasonable agreement with the full-size FMO-LCMO. We called this the FMO with linear combination of valence molecular orbitals (FMO-LCVMO).

For the T_{DA} calculation, we examine the generalized Mulliken-Hush (GMH)[51,52] and the bridge GF methods. For biological ET systems, the one-electron picture based on the Hartree-Fock (HF) Koopmans' theorem (KT)[25–28] is useful and normally sufficient to approximate the T_{DA}-value.[32,33,35,36,47,48,53]

In the HF-KT scheme, the GMH method expresses the T_{DA} in terms of two HF MOs of the whole system, ψ_1 and ψ_2, that mostly contribute to the electron tunneling,[53]

$$T_{\text{DA}} = \frac{|\mu_{12}|\Delta\epsilon_{12}}{\sqrt{(\mu_1 - \mu_2)^2 + 4|\mu_{12}|^2}}, \tag{8}$$

where $\Delta\epsilon_{12}$ is the MO energy difference between ψ_1 and ψ_2. μ_1, μ_2, and μ_{12} are the dipole moment matrix elements, $\langle\psi_1|e\mathbf{r}|\psi_1\rangle$, $\langle\psi_2|e\mathbf{r}|\psi_2\rangle$, and $\langle\psi_1|e\mathbf{r}|\psi_2\rangle$, respectively. Note that, in the KT approximation, the two quasi-degenerate electronic eigenstates of the ET system are expressed by the electronic configurations in which one electron is attached to or removed from the ψ's of the HF wavefunction of the whole system. Therefore, the $\Delta\epsilon_{12}$ and μ's

7

correspond to the energy-splitting and dipole matrix elements of the two adiabatic states, respectively. A major advantage of the GMH method over the ordinary energy splitting method is that it can be applied to any geometry not limited to that corresponding to the transition state.[25,32,33,51–53]

By using the GF method,[23–25,54] we approximate the electronic coupling with the FMO-LC(V)MO calculations as follows:[47]

$$
T_{\mathrm{DA}} = \sum_I^N \sum_J^N \sum_{I_p(\neq \phi_D, \phi_A)} \sum_{J_q(\neq \phi_D, \phi_A)} (E_{\mathrm{tun}} S_{\phi_D, I_p} - H_{\phi_D, I_p})
$$
$$
\times G^B(E_{\mathrm{tun}})_{I_p, J_q} (E_{\mathrm{tun}} S_{J_q, \phi_A} - H_{J_q, \phi_A}) \tag{9}
$$

where ϕ_D and ϕ_A are fragment monomer MOs specified as the donor and acceptor MOs, respectively. The bridge GF is given in the matrix form by

$$
\mathbf{G}^B(E_{\mathrm{tun}}) = [E_{\mathrm{tun}} \mathbf{S}^B - \mathbf{H}^B]^{-1}, \tag{10}
$$

in which $\mathbf{H}^B$ is the bridge part of the FMO-LC(V)MO Hamiltonian matrix in eqs 6 7, $\mathbf{S}^B$ is the corresponding overlap matrix among the non-orthogonal fragment monomer MOs, and E_{tun} is the tunneling energy parameter. In this study, E_{tun} is set to the average value between the donor and acceptor MO energies.

For the ET pathway analysis, we employ the tunneling-current method[15,17,25] within the one-electron picture.[47] We first express the MOs $|\psi^i\rangle$ and $|\psi^f\rangle$ in the initial and final diabatic states in terms of the fragment monomer MOs $|\phi_p^I\rangle$ as follows:

$$
|\psi^i\rangle = C_D^i |\phi_D\rangle + \sum_I^N \sum_{I_p} C_{I_p}^i |\phi_p^I\rangle \tag{11}
$$

$$
|\psi^f\rangle = C_A^f |\phi_A\rangle + \sum_I^N \sum_{I_p} C_{I_p}^f |\phi_p^I\rangle \tag{12}
$$

Because $|C_D^i| \simeq 1$ and $|C_A^f| \simeq 1$ can be assumed in the weak coupling case, the coefficients $C_{L_p}^i$ and $C_{L_p}^f$ are expressed by the bridge GF matrix eq 10 as follows:[15,19,21,25]

$$C_{L_p}^i = -\sum_M^N \sum_{M_q} \left(E_{\text{tun}} S_{\phi_D, M_q} - H_{\phi_D, M_q}\right) G^B(E_{\text{tun}})_{M_q, L_p} \tag{13}$$

$$C_{L_p}^f = -\sum_M^N \sum_{M_q} G^B(E_{\text{tun}})_{L_p, M_q} \left(E_{\text{tun}} S_{M_q, \phi_A} - H_{M_q, \phi_A}\right) \tag{14}$$

The tunneling current J_{L_p, M_q} between the monomer MOs ϕ_p^L and ϕ_q^M is given by[15,19,21,25]

$$J_{L_p, M_q} = \frac{1}{\hbar}(H_{L_p, M_q} - E_{\text{tun}} S_{L_p, M_q})(C_{L_p}^i C_{M_q}^f - C_{L_p}^f C_{M_q}^i). \tag{15}$$

Therefore, the tunneling current between fragments L and M is obtained as

$$J_{L,M} = \sum_{L_p} \sum_{M_q} J_{L_p, M_q}. \tag{16}$$

The electronic coupling calculated from the bridge GF method in eq 9 is rewritten by using the tunneling currents as follows:[15,19,21,25]

$$T_{\text{DA}} = \hbar \sum_{L \in \Omega_D, M \notin \Omega_D} J_{L,M} \tag{17}$$

where Ω_D denotes a properly chosen donor side space. We can visualize the main pathways at fragment-based resolution with the connecting vectors of the following normalized tunneling currents[19–21]

$$K_{L,M} = \hbar(J_{L,M})/T_{\text{DA}}. \tag{18}$$

The advantage of our fragment-based approach over those based on the atomic orbitals (AOs) becomes more apparent as the system size increases, because we directly obtain the Hamiltonian matrix in the fragment MO basis in eqs 6 7 without the need to construct the much larger matrix in the AO basis. As described in the Supporting Information, it

is straightforward to expand the fragment MOs in the AO basis for the analysis of atomic resolution when needed.

COMPUTATIONAL METHODS

Model systems and their structures

Here we describe the model systems for the ET reactions from the bacteriopheophytin b (H_L) anion to Q_A (menaquione, MQ) and from the MQ anion to Q_B (ubiquinone, UQ) in the bacterial photosynthetic RC of *Blastochloris* (*Blc.*) *viridis* (previously called *Rhodopseudomonas viridis*).

The first ET from H_L to MQ is modeled by the system (A) illustrated in Figure 1. The long hydrocarbon chains of native H_L and MQ were replaced by hydrogen atoms. The side chains of H_L that do not conjugate with the π orbitals of the chlorin ring were replaced by hydrogen atoms, except for the methyl group connecting to C12 in the chlorin ring III of H_L. The methyl group is located at the side near the considered bridge and might have the π-conjugated character via hyperconjugation effect.[22] For the potential candidates contributing to the main tunneling pathway, we included the amino acids Ala M215, Ala M216, His M217, and Trp M250 locating between the redox centers. The back-bone amino acid chains were truncated at the C_α atoms of Ala M215, His M217, and Trp M250, and capped by hydrogen atoms for Ala M215 and Trp M250 and capped by methyl group for His M217 as shown in Figure 1(A).

For the second ET from MQ to UQ, we adopted the model systems illustrated in Figure 1 (B) and (C), with and without the divalent metal ion (Fe^{2+} or Zn^{2+}). Here we refer to the previous theoretical studies in which the Fe^{2+} ion was either removed,[39] replaced by Zn^{2+},[37] or modeled only by p-orbitals.[49] We also refer to the experimental study by Debus et al.[55] which observed the ET rates when the Fe^{2+} ion was depleted or replaced by various divalent metal ions including Zn^{2+} in a different bacteria, *Rhodobacter* (*Rba.*) *sphaeroides* R-26.1. In

our model, the long hydrocarbon chains of native MQ and UQ were replaced by hydrogen atoms. The imidazole groups of His M217, His M264, His L190, and His L230 and the side chain of Glu M232 are included as potential candidates for the main tunneling pathway, in which the truncated sites were capped by hydrogen atoms as shown in the Figure. The deprotonated caboxylate form was assumed for the Glu M232 coordinating to the Fe^{2+} ion.

The coordinates of the heavy atoms were taken from the X-ray crystallographic data in the Protein Data Bank, code 1PRC.[56] The coordinates of the hydrogen atoms of system (A) were determined by a geometrical optimization with the semi-empirical PM3 method,[57] in which the neutral singlet state was assumed and the positions of all the heavy atoms were fixed. Similar procedure was applied to system (B), in which the Fe^{2+} ion was replaced by a Zn^{2+} and the cation singlet state was assumed. The coordinates of the hydrogen atoms of system (C) are set identical to those of system (B). These geometrical optimizations were carried out using the Gaussian 09 software, revision B.01.[58]

Electronic structure calculations

Here we detail the HF and FMO2 calculations. The charge and spin states were set to be neutral singlet for (A), cation singlet for (B) with Zn^{2+}, and anion singlet for (C). Since the EPR experiments[59] have suggested that the Fe^{2+} ion located between MQ and UQ in the actual bacterial photosynthetic RCs is in a high-spin ($S = 2$) state, we performed UHF[1] calculation for system (B) with a Fe^{2+} ion in cation quintet state. We also performed RHF and FMO2 calculations for the system (B) with a low-spin Fe^{2+} to examine the effect of spin-state on the T_{DA} value.

For calculating the anion coupling of system (A) with the HF-KT scheme, the obtained LUMO and LUMO+1 orbitals were identified as ψ_1 and ψ_2. The fragments in the FMO calculations are the four covalent-binding blocks, H_L, MQ, {Ala M215 + Ala M216 + His M217}, and Trp M250. Total charge of each fragment was set to 0. For system (A), the

---

[1]The expectation value of the total squared-magnitude of the spin, $\langle S^2 \rangle$, calculated form the UHF calculation was 6.008, which indicating that the obtained result is almost pure spin state.

dimension of FMO-LCVMO Hamiltonian is always reduced to 357 corresponding to the minimal valence space. The dimension of the full FMO-LCMO depends on the basis set and will be noted in the Results section.

For calculating the anion coupling of system (B) with the HF-KT scheme, we used the obtained LUMO and LUMO+1 orbitals as ψ_1 and ψ_2. In the UHF results of system (B) with Fe^{2+} in cation quintet state, the MOs 208 and 209 of α-spin correspond to ψ_1 and ψ_2, respectively. In the RHF results of system (B) with the Fe^{2+}/Zn^{2+} in cation singlet state, the MOs 206 and 207 correspond to ψ_1 and ψ_2, respectively. The fragments used in the FMO calculations are the three blocks, MQ, UQ, and { metal ion (Fe^{2+} or Zn^{2+}) + His M217 + His M264 + His L190 + His L230 + Glu M232 }. Total charges of the fragments MQ and UQ were set to 0 and that for the metal-containing fragment was set to +1. In the case of system (B), the FMO-LCVMO approach always reduces the dimension of the total Hamiltonian to 265.

For calculating the anion coupling of system (C) with the HF-KT scheme, we used the obtained LUMO and LUMO+1 orbitals as ψ_1 and ψ_2. The fragments used in the FMO calculations are the seven covalent-binding blocks, MQ, UQ, His M217, His M264, His L190, His L230, and Glu M232. Total charge of Glu M232 was set to -1 and those for the other six fragments were set to 0. For system (C), the FMO-LCVMO calculation always reduces the dimension of the total Hamiltonian to 255.

The FMO2 calculations were performed using the FMO code[42] implemented in the GAMESS program.[60] All the calculations in this study do not involve bond-detached atoms (BDAs).[41,42] No cut-off for approximating the SCF energy by electrostatic interaction was employed and all pairs of monomers were taken into account for dimer calculations. The HF calculations of the entire non-fragmented system were also performed using the GAMESS program.[60]

Previous studies[26,31,35,36,47] have demonstrated that the split-valence Gaussian-type basis sets are sufficient to describe the super-exchange T_{DA} in organic molecules and protein ETs.

In this study we examined several basis sets including minimum, split-valence, and triple-split valence with and without polarization functions, but the results with the 6-31G(d) set will be presented in the body of the paper. The convergence of the T_{DA} value with respect to the basis set is shown in Figure S1, S3, and S4 in the Supporting Information. Diffuse-function basis set was not employed to avoid the convergence problem in FMO calculation. Although a previous study has noted the need of diffuse-functions when the main tunneling pathways include intermolecular gaps greater than 4 Å,[48] it is not the case for the ETs in this study.

RESULTS

ET from H_L to MQ

For the ET from H_L to MQ in Figure 1 (A), we first confirmed that the deviation between the RHF and FMO2 total energies was 0.210 millihartree (mh) for the 6-31G(d) set, and less than 0.3 mh for the other basis sets. (See Figure S1(a) of the Supporting Information.) Using the FMO2 results, we constructed the FMO-LC(V)MO Hamiltonians. The dimension of the FMO-LCMO Hamiltonian, 1232 with the 6-31G(d) set, was reduced to 357 by the FMO-LCVMO scheme. The canonical MOs of the whole system (A) was obtained by solving the generalized eigenvalues problem of the FMO-LC(V)MO Hamiltonian. As shown in Figure 2, the MO energy spectrum of the full RHF reference was well reproduced in the valence MO range of −40 to 20 eV.

In Figure 3 we draw the LUMO ψ_1 and LUMO+1 ψ_2 of system (A) which are used in the GMH calculation by eq 8. The MO energies ϵ_1 of ψ_1 from the RHF, FMO-LCMO, and FMO-LCVMO calculations were −0.73710, −0.73639, and −0.73614 eV, respectively, represented by the red lines in Figure 2. Similarly, the MO energies ϵ_2 of ψ_2 were 0.50345, 0.50255, and 0.50953 eV, respectively, represented by the blue lines in Figure 2. In Figure 3 we also draw the LUMOs of H_L and MQ fragments to be used as the donor and acceptor orbitals ϕ_D and

ϕ_A. As seen in Figure 3(a), ψ_1 is mostly a π-conjugated orbital on the H_L fragment consisting mainly of ϕ_D. Similarly, Figure 3(b) shows that ψ_2 is mostly a π-conjugated orbital on the MQ fragment consisting mainly of ϕ_A. The calculated T_{DA} values by the GMH method are listed in Table 1, showing that both the FMO-LCMO and FMO-LCVMO reasonably reproduce the reference RHF value. We confirmed that the $|T_{DA}|$ results do not significantly depend on the employed basis sets except for the minimum one, as plotted in Figure S1(b) of the Supporting Information.

We also calculated T_{DA} by the bridge GF method of eq 9 with the FMO-LC(V)MO Hamiltonian. The energies of ϕ_D and ϕ_A, ϵ_D and ϵ_A, were -0.751 eV and 0.553 eV, respectively. Their average, -0.0990 eV, was used for E_{tun}. The results included in Table 1 show reasonable agreement with those from the GMH method. The agreement was checked for all the employed basis sets as shown in Figure S1(b) of the Supporting Information.

The ET rate and its inverse, the ET time, are calculated by using eq 1 with the obtained T_{DA} values. The driving force $-\Delta G$ experimentally evaluated for the native ET from H_L to MQ in the RC of *Blc. viridis* is 0.6 eV.[2,3] The dependence of the ET rate on $-\Delta G$ has been investigated by extraction and replacement of the quinone cofactor,[2,3] by which the reorganization energy λ was estimated to be 0.7 eV. Using these numbers and the T_{DA} results at the 6-31G(d) level, the ET rate k_{DA}^{calc} and the ET time $1/k_{DA}^{calc}$ at $T = 300$ K are calculated and listed in Table 1. The calculated results, $1/k_{DA}^{calc}$ of 263-375 ps, are in reasonable agreement with the observed ET time $1/k_{DA}^{obs}$ of 200 ps.[56]

In Figure 4, we draw the normalized inter-fragment tunneling currents $K_{L,M}$'s by eq 18. The numerical figures near the arrow and in parentheses stand for the corresponding $|K_{L,M}|$ values from the FMO-LCMO and FMO-LCVMO calculations, respectively. We see that these two calculations are consistent with each other. Figure 4 shows that the large $K_{L,M}$'s dominantly flow from H_L through Trp M250 to MQ. This is therefore regarded as the main tunneling pathway for the ET from H_L to MQ. Figure 4 also shows that the small $K_{L,M}$'s flow from MQ to {Ala M215 + Ala M216 + His M217} and then to H_L and Trp M250, leading to

fractional destructive interference. In Figure S2(a) of the Supporting Information, we also draw the map of the normalized inter-atomic tunneling currents by expanding the $K_{L,M}$'s obtained for system (A) in the AO basis.

ET from MQ to UQ

We now carry out similar analysis on the ET from MQ to UQ in Figure 1(B)-(C). In addition to the RHF and FMO2 calculations, we performed the UHF calculations for system (B) with the high-spin Fe^{2+}. The error between the RHF and FMO2 total energies for systems (B) and (C) as a function of the employed basis sets were plotted in Figures S3(a) and S4(a) of the Supporting Information, respectively. Using the results of the FMO2 calculations, we constructed the FMO-LC(V)MO Hamiltonian for each system. In system (B), the dimension of the FMO-LCMO Hamiltonian, 920 with the 6-31G(d) set, was reduced to 265 by the FMO-LCVMO scheme. In system (C), the dimension of the FMO-LCMO Hamiltonian, 881 with the 6-31G(d) set, was reduced to 255 by the FMO-LCVMO scheme. As shown in Figures S5-S7 of the Supporting Information, the MO energy spectrum of the full RHF reference was well reproduced in the valence MO range of -40 to 20 eV, for each the system.

By using the GMH calculation, eq 8, we next calculated the T_{DA}'s of system (B) with the high-spin and low-spin Fe^{2+}. In Figure 5 we draw the LUMO ψ_1 and LUMO+1 ψ_2 from the UHF calculation of system (B) with the high-spin Fe^{2+}. (In Figures S5(b) of the Supporting Information, we plot the MO energy spectra obtained from the UHF calculation.) In Figure 5 we also draw the LUMOs of MQ and UQ fragments used as the donor and acceptor orbitals ϕ_D and ϕ_A. The ψ_1's obtained from the UHF and RHF calculations are similar to each other and to ϕ_A. Similarly, the ψ_2's obtained from the UHF and RHF calculations are similar to each other and to ϕ_D. (See Figure 5 and Figure S8 of the Supporting Information.) The calculated $|T_{DA}|$ values by the GMH method are listed in Table 2, showing the both the FMO-LCMO and FMO-LCVMO reasonably reproduce the reference RHF value for system (B) with the low-spin Fe^{2+}. We also confirmed that the $|T_{DA}|$ results do not significantly

depend on the employed basis sets except for the minimum one, as plotted in Figure S3(b) of the Supporting Information. Interestingly, Table 2 also shows that the $|T_{\text{DA}}|$ does not depend much on the spin state; the high-spin/low-spin ratio is only 1.41.

By using eq 8, we next calculated the T_{DA}'s of system (B) with the Zn^{2+} and (C). In Figures S9 and S10 of the Supporting Information, we draw the ψ_1's and ψ_2's of these systems. For each the system, the ψ_1 and ψ_2 are similar to the FMOs ϕ_A and ϕ_D, respectively. Table 2 lists the T_{DA}'s obtained from eq 8 with the RHF, FMO-LCMO, and FMO-LCVMO calculations for each the system. (These are plotted as functions of the employed basis sets in Figures S3(c) and S4(b) of the Supporting Information, respectively.) It shows that both the FMO-LCMO and FMO-LCVMO calculations reasonably reproduce the reference $|T_{\text{DA}}|$'s from RHF calculations, irrespective of the presence of the metal ion. Table 2 also shows the T_{DA}'s for system (B) with the Zn^{2+} are close to those for system (B) with the high-spin Fe^{2+}, and that the presence of the metal ion increases the $|T_{\text{DA}}|$ value by a factor up to 2.2.

We also calculated T_{DA} by the bridge GF method of eq 9 with the FMO-LC(V)MO Hamiltonian. For system (B) with the low-spin Fe^{2+}, the energies ϵ_D and ϵ_A of ϕ_D and ϕ_A, were -1.08 eV and -1.48 eV, respectively, and the tunneling energy, E_{tun}, was set to their average, -1.28 eV. For system (B) with the Zn^{2+}, ϵ_D and ϵ_A were -1.08 eV and -1.50 eV, respectively, and E_{tun} was set to their average, -1.29 eV. For system (C), ϵ_D and ϵ_A were 2.06 eV and 2.00 eV, and E_{tun} was set to their average, 2.02 eV. The results in Table 2 show reasonable agreement with those from the GMH method in eq 8 for each the system. The agreement was checked for all the employed basis sets as shown in Figures S3(c) and S4(b) of the Supporting Information.

We next calculated T_{DA} of system (B) with the high-spin Fe^{2+} by the bridge GF method. Since the the FMO-LCMO method has not been implemented for open-shell system, one-electron Hamiltonian of the open-shell system required for the bridge GF calculation with eq 9 cannot be constructed only from FMO result. Instead, by using the obtained UHF result, we constructed one-electron Hamiltonian of the high-spin Fe^{2+} system in the fragment

monomer MO basis as follows: A i-th canonical MO of α-spin electron and its energy from the UHF calculation are represented by $|\psi_i\rangle$ and ϵ_i, respectively. The fragment monomer MOs, ϕ_p^L, of system (B) with the low-spin Fe^{2+} are used to expand the total Hamiltonian of the high-spin system as follows:

$$H_{L_p,M_q}^{\text{UHF}} = \sum_i^{\text{all}} \langle \phi_p^L | \psi_i \rangle \epsilon_i \langle \psi_i | \phi_q^M \rangle. \tag{19}$$

The LUMOs of MQ and UQ fragments were again adopted as ϕ_D and ϕ_A, respectively. The E_{tun} was also set to the same value used for the low-spin case. The T_{DA} for system (B) with the high-spin Fe^{2+} was calculated by using the bridge GF method of eq 9 with eq 19 in the same manner as that with FMO-LCMO Hamiltonian. As listed in Table 2, the resultant T_{DA} is also in reasonable agreement with that from the GMH method in eq 8 for system (B) with the high-spin Fe^{2+}. The Hamiltonian, H_{L_p,M_q}^{UHF}, was used in the subsequent tunneling-current anaysis for the high-spin Fe^{2+} case, as described later.

With these T_{DA} values, the ET rates and ET times are calculated using eq 1. The driving force $-\Delta G$ experimentally evaluated for the native ET from MQ to UQ in *Blc. viridis* is 0.07 eV.[2,3] The reorganization energy λ for the ET from Q_A^- to Q_B in the bacterial RC has been estimated to be 0.85-1.1 eV.[3,61,62] (This large uncertainty about λ is attributed to difficulty in observing $-\Delta G$-dependence of the intrinsic ET rate, which will be described in detail in the following section.) Following the work by Moser et al.,[3] we used $\lambda = 1.0$ eV in this study. Using these numbers and the T_{DA} results at 6-31G(d) level, $k_{\text{DA}}^{\text{calc}}$ and $1/k_{\text{DA}}^{\text{calc}}$ at $T = 300$ K are calculated for systems (B) and (C) and listed in Table 2. Because the ET rate from eq 1 is proportional to $|T_{\text{DA}}|^2$, $k_{\text{DA}}^{\text{calc}}$'s for system (B) with the Zn^{2+} or high-spin Fe^{2+} are faster by a factor of ca. 5 than those for system (C). The results $1/k_{\text{DA}}^{\text{calc}}$ of 10 μs from the UHF calculation, are in reasonable agreement with $1/k_{\text{DA}}^{\text{obs}}$ of 25-36 μs (half-time of 17-25 μs).[63,64]

In order to analyze the tunneling pathways, the $K_{L,M}$'s of systems (B) and (C) were calculated. Note that the $K_{L,M}$'s for the high-spin Fe^{2+} case were calculated with the UHF

17

Hamiltonian, $H_{L_p, M_q}^{\text{UHF}}$, of eq 19 instead of FMO-LCMO Hamiltonian. The $K_{L,M}$-map of system (C) shows the contribution of each amino acid residues to the electron tunneling. On the other hand, because the metal-ligand complex had to be treated as a single fragment to achieve convergence, the fragment-based analysis could not gain sufficient resolution. In such cases, the analysis based on the normalized inter-atomic tunneling currents $K_{a,b}$'s is useful. The results for systems (B) with low-spin Fe^{2+} and Zn^{2+} are plotted in Figure 6(a) and (b), respectively. Figure 6 shows that large $K_{a,b}$'s circle around the imidazole rings of His M217 and His L190 and flow from the metal ion to the imidazole rings and vice versa. Most of them cancel each other and the residual currents flowing from donor and to acceptor contribute to the total T_{DA} as shown in eq 17. To show the flow of such important currents clearly and to compare with the $K_{L,M}$-map of the system (C), we sum the $K_{a,b}$'s of systems (B) as follows:

$$K_{\text{Res}X,\text{Res}Y} = \sum_{a \in \text{Res}X} \sum_{b \in \text{Res}Y} K_{a,b} \tag{20}$$

where Res X represents MQ, UQ, His M217, His M264, His L190, His L230, Glu M232, or Fe^{2+}/Zn^{2+}. In Figure 7 (a)-(c), we draw the $K_{\text{Res}X,\text{Res}Y}$'s of system(B) with the high-spin Fe^{2+}, low-spin Fe^{2+}, and Zn^{2+}, respectively. In Figure 8, we draw the $K_{L,M}$-map of system (C). (In Figure S2(b) of the Supporting Information, we also draw the $K_{a,b}$-map of system (C).) Figure 8 shows that the $K_{L,M}$ maps from the FMO-LCMO and FMO-LCVMO calculations are consistent with each other. For system (C), the large $K_{L,M}$ first flow from MQ to His M217, then flow to His L190, and lastly reaches UQ, as shown in Figure 8. The sequence of the large $K_{L,M}$'s can therefore be regarded as the main tunneling pathway for the ET from MQ to MQ without the metal ion. Figure 8 also shows that the $|K_{L,M}|$'s related to His M264, His L230, and/or Glu M232 are less than 0.1 and cause fractional destructive interferences to the main tunneling pathway. On the other hand, for systems (B), the large currents flow through His M217, His L190, and the metal ion. Figure 7(a) and (b) show that $K_{\text{MQ},Fe^{2+}}$ and $K_{\text{UQ},Fe^{2+}}$ are large, leading to the increase in the back-flow of the tunneling currents for the ET from MQ to UQ with the low-spin Fe^{2+}. Figure 7(c)

shows that $K_{\mathrm{MQ,Zn^{2+}}}$ and $K_{\mathrm{UQ,Zn^{2+}}}$ are smaller than $K_{\mathrm{MQ,Fe^{2+}}}$ and $K_{\mathrm{UQ,Fe^{2+}}}$, which suppresses the destructive interference via the metal ion. From Figures 7 and 8, the presence of the metal ion increases the currents via the residues, His M264, His L230, and Glu M232, which slightly enhances the destructive interference.

DISCUSSION

Assessment of the approach

As described in the Results section, our approach with the GMH and bridge GF methods with the FMO-LC(V)MO Hamiltonian produced the T_{DA} values consistent with each other and in good agreement with the reference all-electron calculations. This supports the validity of the subsequent tunneling pathway analyses and ET rate calculations.

The use of the size-reduced FMO-LCVMO method in our approach is the key to reducing the computational cost. Its agreement with the full FMO-LCMO calculation shows its promise for studying realistic protein ETs at the *ab initio* QM quality.

The T_{DA}'s obtained for systems (B) are larger than those for system (C). Figures S5-S7 show that the presence of the metal ion results in shifting the ϵ_D/ϵ_A from the center of the band gap of the bridge MO energies to the position near the energy bands of the bridge virtual MOs, leading to the increase in the T_{DA}'s calculated from the GMH method, eq 8. This difference in the obtained T_{DA}'s will be reexamined below in the context of tunneling pathway analysis.

The bridge GF method, eq 9, and the subsequent pathway analysis with eq 18 involve the tunneling energy parameter E_{tun}. In this study, E_{tun} was set to the average values of the donor and acceptor MO energies, $(\epsilon_D + \epsilon_A)/2$. Previous studies have shown the choice of E_{tun} value may remarkably affect the results for some cases.[54] We have examined this issue and confirmed little dependence in the relevant region of E_{tun} for all the cases in this study, as illustrated in Figure S11 of the Supporting Information.

For most typical protein ET systems the T_{DA} values are as small or less than 1.0 cm^{-1}, as those obtained in this study. One might be concerned about the quantitative reliability of our approach based on the HF-MOs/FMOs and their energies to calculate such small T_{DA}'s. When T_{DA}'s less than 10^{-3} cm^{-1} is calculated, directly using the MO energy splitting method (and the GMH method involving that) was considered inadequate due to the numerical difficulties discussed well in Refs. 25,38. By contrast, our previous study[47] have demonstrated that both the MO energy splitting and bridge GF methods reproduce reliable T_{DA} values for the organic model systems with symmetric structures in the regions of 10^3 - 10^{-3} cm^{-1}. Therefore, for the regions of the T_{DA}'s in this study, our method is expected to reproduce reasonable results within the framework of the HF-KT scheme.

Although the HF-KT scheme ignores electron correlation effect, many previous theoretical studies[32,33,35,36,47,48,53] demonstrated that the scheme is normally sufficient to approximate T_{DA} for protein ET. For most of small model ET systems studied so far, the effect of electron correlation is known to be small; since the errors arising from electron correlation and orbital relaxation in the T_{DA} tend to cancel each other, the HF-KT scheme well reproduces the T_{DA}'s from the post-HF methods.[28,31,65] Yang and Hsu[66] have precisely shown that the dynamical correlation effect is sufficiently small by using coupled-cluster single and double (CCSD) method. We have previously demonstrated that the main tunneling pathways through the localized MOs in HF-KT calculations well correspond to those in MCSCF calculations which adequately take into account both effects of non-dynamical electron correlation and orbital relaxation.[31] All these support our method based on (localized) monomer fragment MOs in the HF-KT picture to describe the adequate tunneling pathways.

In a similar way to the previous studies[39,50] on the ETs in RCs we adopted the LUMO and LUMO+1 of the whole system as ψ_1 and ψ_2 in the GMH method and the LUMOs of the donor and acceptor fragments as ϕ_D and ϕ_A in the bridge GF and subsequent tunneling current methods. For some organic ETs, the T_{DA}'s from the HF-KT scheme with the LUMOs as ψ_1 and ψ_2 are reasonably consistent with those from post-HF methods.[65,66] In general,

the HF-KT scheme offers multiple options to choose the HF wavefunction; then one can naturally adopt the two MOs from the chosen HF wavefunction as ψ_1 and ψ_2.[28] Alternatively to our present choices, we might have used the HOMO and HOMO-1 of α-spin of the UHF wavefunctions solved for the dianion triplet state of system (A), for anion septet state of system (B) with high-spin Fe^{2+}, for anion triplet state of system (B) with Zn^{2+}, and for trianion triplet state of system (C) to describe to the corresponding ETs. Although these alternatives may seem rather adequate in the sense that occupied orbitals are generally more reliable than virtual ones in SCF calculation, our choices are due to the following reasons: the UHF results contained spin-contamination and the their HOMO and HOMO-1 formed inadequately distorted π-orbitals of H_L, MQ, or UQ. Another practical (and tentative) reason is that the FMO-LCMO method has not been established for open-shell system.

Effect of Fe^{2+}/Zn^{2+}-Ligand Complex on T_{DA} of ET from H_L^- to MQ

System (A) for the ET from H_L^- and MQ does not include the influence from the metal-ligand complex in system (B), { (Fe^{2+} or Zn^{2+}) + His M217 + His M264 + His L190 + His L230 + Glu M232 }, except for M217. This was initially chosen because the complex is located outside the volume between H_L and MQ. However, the experimental study by Kirmaier et al.[67] has shown that the depletion of Fe^{2+} decreases the ET rate from H_L^- and MQ by a factor of 20 - 50, whereas the Zn^{2+}-replacement reproduces the native ET rate. Computational study based on the Poisson-Boltzmann equation has indicated that the electric field arising from the positive charges of Fe^{2+} or Zn^{2+} considerably decreases the redox potential of Q_A, causing the large differences of the $-\Delta G$ in eq 1 between native/Zn^{2+}-replaced RC and Fe-depleted RC.[68] In addition to the effect on $-\Delta G$, the strong electric field has the possibility of affecting the T_{DA} and tunneling pathways via the changes in the shapes of the MOs and their energies, especially for ϕ_A near to the complex.

To elucidate the effects of the metal ion on the ET from H_L^- and MQ , we have considered additional two model systems that extend the model system (A); one includes the Zn^{2+}-ligand

complex of system (B) and the other includes atomic partial charges of the Fe^{2+}-ligand complex (taken from Ref. 69) except for His M217. Hereafter, we call the former "system (A) + Zn-complex" and the latter "system (A) + point charges of Fe-complex". In the RHF calculation for system (A) + Zn-complex, the charge and spin states were set to be cation singlet. In the FMO calculation for system (A) + Zn-complex, the fragments are the four covalent-binding blocks, H_L, MQ, { Ala M215 + Ala M216 + Zn-complex }, and Trp M250. Total charge of the { Ala M215 + Ala M216 + Zn-complex } fragment was set to +1 and those of the other fragments were set to 0. The RHF/FMO calculations for system (A) + point charges of Fe-complex were performed as same ways as those for system (A) described in COMPUTATIONAL METHODS section.

The canonical MO energy spectra of the entire system and monomer MO energy spectra obtained for these extended models are plotted in Figure S12 of the Supporting Information. In Figure 9, we compare their T_{DA} values with those for system (A). Figure 9 shows that the GMH and bridge GF methods performed for each system produced the T_{DA} values consistent with each other. For systems (A), (A) + Zn-complex, and (A) + point charges of Fe-complex, the RHF calculations provided the ϵ_1 of -0.737 eV, -1.55 eV and -1.22 eV, respectively, and the ϵ_2 of 0.503 eV, -0.901 eV and -0.152 eV, respectively. Likewise, the FMO calculations provided the ϵ_D of -0.751 eV, -1.55 eV, and -1.21 eV, respectively, and the ϵ_A of 0.553 eV, -0.857 eV, and -0.196 eV, respectively. The positive charges from the metal-ligand complex considerably reduces the energies of ϕ_2 and ϕ_A on MQ. Although the $\Delta\epsilon_{12}$ used in eq 8 varies from 0.649 eV to 1.24 eV, the GMH method results in little difference in T_{DA} among these systems as shown in Figure 9, demonstrating the adequacy of its scaling idea by the dipole matrix elements. Similarly, the bridge GF method with FMO-LC(V)MO Hamiltonian also results in little difference in T_{DA} among these systems. In Figure S13 of the Supporting Information, we draw $K_{L,M}$'s by eq 18 for the extended systems. We found that the map of $K_{L,M}$'s does not depend on the presence of the metal-ligand complex, by comparing Figure S13 with Figure 4. We therefore conclude that the strong electric field of

the metal-ligand complex does not much affect the T_{DA} and tunneling pathways for the ET from H_L^- and MQ in contrast to $-\Delta G$.

Effects of Protonation Changes of Histidines on T_{DA} of the ET from MQ$^-$ to UQ in Fe-depleted RC

We constructed system (C) only by removing the metal from system (B). Although the four histidines (His M217, His M264, His L190, and His L230) and one glutamate (Glu M232) coordinating the non-heme iron are non-titratable in the native RC, the depletion of Fe makes these groups titratable and have the possibility of changing their protonation states. Ishikita and Knapp[68] have shown that the histidines corresponding to His M217, His M264, and His L230 become protonated by ~ 0.4 H$^+$ upon formation of Q$_A^-$ in the Fe-depleted RC of *Rba. sphaeroides* by using a Monte Carlo method with the electrostatic continuum model. To elucidate the effects of such protonation changes on the ET from MQ$^-$ to UQ, we considered another model systems where both N$_{\delta 1}$ and N$_{\epsilon 2}$ are protonated for each four histidines of system (C). In the RHF calculations, the charge and spin states were set to be neutral singlet. The fragments used in the FMO calculations are the three blocks, MQ, UQ, and { His M217 + His M264 + His L190 + His L230 + Glu M232 }. Total charges of all the fragments were set to 0. The T_{DA}'s obtained from the GMH and bridge GF methods are plotted in Figure S14 of the Supporting Information. We found that the T_{DA}'s calculated for system (C) with protonated His M217 are $0.773 \sim 0.820$ cm^{-1}, larger than those for system (C) by a factor of 1.25. (See Table 2.) Substituting these T_{DA}'s into eq 1 with $\lambda = 1.0$ eV and $-\Delta G = 0.07$ eV used for systems (B) and (C), yield the k_{DA}^{calc} of ca. 4.0×10^4 s^{-1} and $1/k_{DA}^{calc}$ of 25 μs at $T = 300$ K for system (C) with protonated His M217. The T_{DA}'s calculated for the other cases are comparable with those for system (C). Figure S15 of the Supporting Information shows the maps of $K_{L,M}$'s by eq 18 for system (C) with the protonated state of each histidine, indicating that the changes in the protonation states of the histidines do not affect the tunneling pathway from MQ to UQ in the Fe-depleted RC.

Comparison with Observed ET Rates

Experimental studies have shown that the ETs from H_L to MQ and from MQ to UQ in the RC of *Blc. viridis* occur within ca. 200 ps and within 25 to 36 μs, respectively, at room temperature.[56,63,64] The calculated ET times $1/k_{DA}^{calc}$'s for system (A) are 263 - 375 ps, as listed in Table 1. The $1/k_{DA}^{calc}$'s for system (B) with the high-spin Fe^{2+} are ca. 10 μs from the UHF calculation, as listed in Table 2. The degree of agreement in both cases indicates the accuracy of the present approach, and suggests small rearrangement of protein conformation and minor effects from the environmental electrostatic perturbation from outside the model systems.

Next we will focus on the effect of the metal ions on the $1/k_{DA}^{calc}$'s for the ETs from MQ to UQ. Debus et al. examined the ETs from Q_A^- to Q_B in the RCs of *Rba. sphaeroides* R-26.1 in which the Fe^{2+} was removed and/or replaced by a Zn^{2+}.[55] Table 2 lists $1/k_{DA}^{obs}$'s observed in the RC of *Blc. viridis* and the RCs of *Rba. sphaeroides* R-26.1. The $1/k_{DA}^{obs}$ of 150 μs in native RC of *Rba. sphaeroides* R-26.1 is slower by a factor of 6.5-8.8 than that in the native RC of *Blc. viridis*. The $1/k_{DA}^{obs}$ observed in the RC in which the Fe^{2+} is depleted is slower by only a factor of ca. 2 than the $1/k_{DA}^{obs}$ observed in the native RC, as listed in Table 2. The $1/k_{DA}^{obs}$ observed in the RC in which the Fe^{2+} is replaced by the Zn^{2+} is almost same as that observed in the native RC, as listed in Table 2. We found that the $1/k_{DA}^{calc}$ from the UHF calculation for system (B) with the high-spin Fe^{2+} is almost same as the $1/k_{DA}^{calc}$'s for system (B) with the Zn^{2+}, in good agreement with the experimental result. The $1/k_{DA}^{calc}$'s for system (B) with the low-spin Fe^{2+} are slower by only a factor of ca. 2 than that for system (B) with the high-spin Fe^{2+}. As listed in Table 2, we found that the $1/k_{DA}^{calc}$'s for the system (C) are slower by a factor of ca. 5 than that for system (B) with the high-spin Fe^{2+}, which also reasonably agrees with the experimental result. As described in the previous subsection, the $1/k_{DA}^{calc}$'s for the system (C) with protontated His M217 are slower by a factor of ca. 3 than that for system (B) with the high-spin Fe^{2+}, which reproduces the experimental result more than those for system (C). Although the relaxation of the protein conformation caused

by the extraction and/or replacement of the metal ion was neglected in the calculation, the behavior of $1/k_{DA}^{calc}$ reasonably corresponds to that of $1/k_{DA}^{obs}$.

It has been believed previously[61,70–72] from the experimental findings listed below that the ET rate from Q_A^- to Q_B in bacterial photosynthetic RC is limited by protein conformational change responding to the reduction of Q_A rather than the electron tunneling: (1) The ET from Q_A^- to Q_B can proceed in RCs frozen under the light in contrast to that in RCs frozen in the dark.[70,71] (2) The X-ray crystallographic study of *Rba. sphaeroides* RCs at cryogenic temperature has shown that the Q_B located at the distal position in the dark moves ca. 4.5 Å with a 180° "propeller twist" toward the proximal position in the RCs frozen under illumination.[72] (3) The observed rate of this ET in *Rba. sphaeroides* RC at room-temperature is independent of the $-\Delta G$ over a range of 150 meV.[61] Therefore, the well-characterized $1/k_{DA}^{obs}$ of ca. 100 μs in *Rba. sphaerodies* RC has been considered to correspond to the confromational gating time for this ET. At first, it was proposed that the large displacement of neutral Q_B, the finding (2) above, before the occurrence of the electron tunneling is the conformational gating step for this ET.[61,72] However, recent experimental studies[71,73–75] have shown that such a large motion of neutral Q_B before the electron tunneling cannot occur. (The systems (B) and (C) used in this study possess the UQ in the proximal Q_B binding site, as shown in Figure 1.[56,75]) Thus, there is no consensus about which protein conformational changes correspond to the conformational gating step. At first, a little dependence of $1/k_{DA}^{obs}$ on the metal ion observed by Debus et al.[55] had been interpreted as a negligible contribution of the metal's electronic states to the main tunneling pathways from Q_A to Q_B. Since the experimental findings (1)-(3), the little dependence has been believed to be due to the rate-limiting conformational gating step. Interestingly, our results of $1/k_{DA}^{calc}$'s in Table 2 reasonably reproduced such a little dependence on the metal ion of $1/k_{DA}^{obs}$, despite they correspond to the rate of the intrinsic ET time.

The agreement between $1/k_{DA}^{calc}$ and $1/k_{DA}^{obs}$ for systems (B)-(C) does not necessarily contradict the conformational gating mechanism for the ET from Q_A^- to Q_B. By observing the

time-resolved change of the difference spectrum of Q_A^- minus Q_B^- absorption, Li et al.[76] have found a fast component, τ_1, of 3-6 μs in addition to the well-recognized component, τ_2, of 100 μs for this ET in *Rba. sphaeroides* RC where the native ubiquinone Q_A was replaced by naphthoquinones. Li et al.[62] have also found that the τ_1 decreased from 29 to 0.2 μs as $-\Delta G$ was modified from -90 to -250 meV by mutation of the M265 residue, wheares the τ_2 is independent of $-\Delta G$. From these results, Li et al.[62,76] conclude that τ_1 is the ET time and τ_2 is the conformation gating time. The *Rba. sphaeroides* RC, in which the native Q_A is replaced by naphthoquinones, have almost the same donor, acceptor, and bridges compounds for the ET from MQ^- to UQ in native *Blc. viridis* RC. The $1/k_{DA}^{obs}$ of 25-36 μs in native *Blc. viridis* RC[63,64] is close to τ_1 rather than τ_2 and the weak pH-dependence of $1/k_{DA}^{obs}$[63,64] also corresponds to that of τ_1.[62,76] From these experimental findings, we consider that our results of $1/k_{DA}^{calc}$ produced resonable intrinsic ET times.

Tunneling Pathways Analysis

Finally, we discuss the tunneling pathways. The $K_{L,M}$-map in Figure 4 indicates that Trp M250 plays significant role as a bridge for the electron tunneling from H_L to MQ. Previous theoretical studies have also found the importance of the corresponding Trp residue in both the *Blc. viridis* and *Rba. sphaeroides* RCs.[20,22,39,49,50] While we believe that the present analysis is the most reliable, the qualitative agreement of the different theoretical treatments seems natural since only the Trp M250, among the other nearby residues, has an aromatic side chain which possesses π MOs with the energies close to the ϵ_D and ϵ_A. In addition, the Trp M250 is conserved in the other bacterial photosynthetic RC of *Rba. sphaeroides* and in the photosystem II of *Thermosynechococcus elongatus* and of *Thermosynechococcus vulcanus*.

The $K_{ResX,ResY}$-maps, calculated by using eq 20 and drawn in Figure 7(a)-(c), indicate that His M217, His L190, and the Fe^{2+} / Zn^{2+} play significant role as a bridge for the electron tunneling from MQ to UQ. The $K_{L,M}$-map in Figure 8 indicates that only His M217 and

His L190 play significant role as a bridge for the electron tunneling in the metal-depleted RC. Since His M217 and His L190 are hydrogen bonded to MQ and UQ, respectively, the importance of these residues seems natural. This has been recognized also in the previous studies,[39,49] but the role of the metal ions has not been properly appreciated. Furthermore, the little dependence of $k_{\mathrm{DA}}^{\mathrm{calc}}$ and $k_{\mathrm{DA}}^{\mathrm{obs}}$ on the presence of the metal ion, as listed in Table 2, appears to support the disregard of metal ions in the ET pathway. However, in fact Figures 6−8 demonstrate that the large tunneling currents flow through the Fe^{2+} / Zn^{2+}. This issue will be revisited below.

We again discuss the difference in the T_{DA}'s obtained for systems (B)-(C) in terms of the tunneling-current map with eq 17. The T_{DA} for system (B) with the high-spin Fe^{2+} is larger by a factor of ca. 1.4 than that with the low-spin Fe^{2+}, as listed in Table 2. By comparing Figure 7(a) with Figure 7(b), we see that the presence of the low-spin Fe^{2+} enhances the amplitudes of back-flow currents, such as $K_{\mathrm{UQ,Fe^{2+}}}$, $K_{\mathrm{Fe^{2+},HisM217}}$. Thus, this increase in destructive interference effect decreases the T_{DA} for the low-spin Fe^{2+} case, compared with the high-spin Fe^{2+} case. The T_{DA} with the low-spin Fe^{2+} is smaller by a factor of ca. 0.7 than that with the Zn^{2+}, as listed in Table 2. By comparing Figure 7(a)-(b) with Figure 7(c), we see that the replacement of Fe^{2+} with Zn^{2+} increases the amplitude of $K_{\mathrm{MQ,HisM217}}$ and decreases the amplitudes of the currents involving the metal ion, leading to suppression of the destructive interference. Thus, this change in quantum interference effect cause the difference in the T_{DA}'s of system (B). The T_{DA} for system (C) is smaller than those for system (B) with the Fe^{2+}/Zn^{2+}, as listed in Table 2. By comparing Figure 7 with Figure 8, we can see that the presence of the Fe^{2+}/Zn^{2+} enhances the destructive interference among the tunneling pathways, which mainly arises from the currents involving His M217, His L190, and the metal ion. This enhancement of the destructive interference may seem to conflict with the increase in the T_{DA}. Nevertheless, the tunneling pathways opened by the metal ion increase the amplitude of each tunneling current, $T_{\mathrm{DA}}K_{\mathrm{ResX,ResY}}/\hbar$, which leads to the increase in the overall T_{DA} via eq 17.

CONCLUDING REMARKS

We have applied our approach to ET pathway analysis based on the FMO-LCMO method to the model systems of ETs in the *Blc. viridis* RC shown in Figure 1. The GMH method, eq 8, and the bridge GF method, eq 9, with the FMO-LC(V)MO Hamiltonian were used to calculate the T_{DA}'s. We found that the GMH and bridge GF methods produced consistent T_{DA} values for each the system, as shown in Tables 1 and 2. We also found that the T_{DA}'s calculated with the FMO-LC(V)MO Hamiltonian were in good agreement with the reference all-electron calculations.

By substituting the T_{DA}'s obtained at the 6-31G(d) level and the λ and $-\Delta G$ parameters typically used for the ETs into the semi-classical Marcus formula eq 1, we calculated the ET rate, k_{DA}^{calc}, and ET time, $1/k_{DA}^{calc}$. The $1/k_{DA}^{calc}$ of 263-375 ps, listed in Table 1, are in good agreement with the observed ET time $1/k_{DA}^{obs}$ of 200 ps for the ET from H_L^- to MQ. The $1/k_{DA}^{calc}$ of 8.68-9.48 μs from the UHF calculation for system (B) with the high-spin Fe^{2+} is in reasonable agreement with the $1/k_{DA}^{obs}$ of 25-36 μs for the ET from MQ^- to UQ, as shown in Table 2. The replacement of the high-spin Fe^{2+} by Zn^{2+} or its removal affects the $1/k_{DA}^{calc}$'s by a factor smaller than 4.5, which reproduces the experimental results by Debus et al..[55] Moreover, we have found that the spin state of Fe^{2+} affects the $1/k_{DA}^{calc}$'s by a factor smaller than 2.9.

We have analyzed the tunneling pathways by using the normalized inter-fragment tunneling currents, $K_{L,M}$'s (eq 18), normalized inter-atomic tunneling currents, $K_{a,b}$, and their summation over each fragment, $K_{ResX,ResY}$ (eq 20). For the ET from H_L to MQ, we found that Trp M250 dominantly contributes to the tunneling pathways, as shown in Figure 4. For system (C), we found that the large $K_{L,M}$ first flow from MQ to His M217, then flow to His L190, and lastly reaches UQ, as shown in Figure 8. On the other hand, for systems (B), we found that the large tunneling currents dominantly flow through the Fe^{2+}/Zn^{2+} in addition to the two His residues, as shown in the $K_{a,b}/K_{ResX,ResY}$-maps of Figures 6−8. This is the first *ab initio* MO study on the role of metal ions in the electron tunneling pathway from

Q_A^- to Q_B in RC.

Another important aspect is that our approach succeeded to analyze systems with non-symmetric and inhomogeneous bridges. When the realistic protein ET system with over several hundreds atoms is considered in the electronic structure calculations, the size-reduced FMO-LCVMO method will become increasingly crucial to reduce the computational cost for the T_{DA} calculation and the subsequent tunneling-pathway analysis. For systems (A)-(C), the FMO-LCVMO method produced the reasonable T_{DA}'s and $K_{L,M}$'s for all cases in comparison with the full-size FMO-LCMO method, as shown in Tables 1 and 2 and Figures 4 and 8. Therefore, the approach is reliable and versatile to study realistic protein ETs with *ab initio* QM quality.

Acknowledgement

Supporting Information Available

Derivation of inter-atomic tunneling currents from FMO-LC(V)MO calculations, basis set dependence of the errors in the total energies and T_{DA} for systems (A)-(C), maps of normalized inter-atomic tunneling currents $K_{a,b}$ for systems (A) and (C), canonical MO energy spectra of the entire system and monomer MO energy spectra for systems (B),(C), (B) + Zn-complex, and (B) + point charges of Fe-complex, frontier MOs for systems (B)-(C), maps of $K_{L,M}$ obtained for systems (B) + Zn-complex and (B) + point charges of Fe-complex, and (C) with each protonated His, $|T_{DA}|$ obtained for systems with each protonated His, and dependence of $|T_{DA}|$ from eq 9 on the E_{tun}.

This material is available free of charge via the Internet at `http://pubs.acs.org/`.

References

(1) Marcus, R. A.; Sutin, N. Electron transfers in chemistry and biology. *Biochim. Biophys. Acta* **1985**, *811*, 265.

(2) Moser, C. C.; Keske, J. M.; Warncke, K.; Farid, R. S.; Dutton, P. L. *Nature* **1992**, *355*, 796.

(3) Moser, C. C.; Page, C. C.; Farid, R.; Dutton, P. L. *J. Bioene. Biomemb.* **1995**, *27*, 263.

(4) Winkler, J. R.; Di Bilio, A. J.; Farrow, N. A.; Richards, J. H.; Gray, H. B. *Pure Appl. Chem.* **1999**, *71*, 1753.

(5) Gray, H. B.; Winkler, J. R. Long-range electron transfer. *Proc. Natl. Acad. Sci. USA.* **2005**, *102*, 3534.

(6) Farver, O.; Pecht, I. *Coord. Chem. Rev.* **2011**, *255*, 757.

(7) McConnell, H. M. *J. Chem. Phys.* **1961**, *35*, 508.

(8) Beratan, D. N.; Betts, J. N.; Onuchic, J. N. *Science* **1991**, *252*, 1285.

(9) Kuki, A.; Wolynes, P. G. *Science* **1987**, *236*, 1647.

(10) Page, C. C.; Moser, C. C.; Chen, X.; Dutton, P. L. Natural engineering principles of electron tunnelling in biological oxidation-reduction. *Nature* **1999**, *402*, 47.

(11) Jones, M. L.; Kurnikov, I. V.; Beratan, D. N. *J. Phys. Chem. A* **2002**, *106*, 2002.

(12) Regan, J. J.; Di Bilio, A. J.; Langen, R.; Skov, L. K.; Winkler, J. R.; Gray, H. B.; Onuchic, J. N. *Chem. Biol.* **1995**, *2*, 489.

(13) Siddarth, P.; Marcus, R. A. *J. Phys. Chem.* **1993**, *97*, 2400.

(14) Skourtis, S. S.; Beratan, D. N. Electron Transfer Contact Maps. *J. Phys. Chem. B* **1997**, *101*, 1215.

(15) Stuchebrukhov, A. A. Tunneling currents in electron transfer reaction in proteins. II. Calculation of electronic superexchange matrix element and tunneling currents using nonorthogonal basis sets. *J. Chem. Phys.* **1996**, *105*, 10819.

(16) Stuchebrukhov, A. A. *Adv. Chem. Phys.* **2001**, *118*, 1.

(17) Stuchebrukhov, A. A. *J. Chem. Phys.* **2003**, *118*, 7898.

(18) Hayashi, T.; Stuchebrukhov, A. A. Electron tunneling in respiratory complex I. *Proc. Natl. Acad. Soc.* **2010**, *107*, 19157.

(19) Kawatsu, T.; Kakitani, T.; Yamato, T. Worm Model for Electron Tunneling in Proteins: Consolidation of the Pathway Model and the Dutton Plot. *Inorg. Chim. Acta.* **2000**, *300-302*, 862.

(20) Nishioka, H.; Kimura, A.; Yamato, T.; Kawatsu, T.; Kakitani, T. Interference, Fluctuation, and Alternation of Electron Tunneling in Protein Media. 1. Two Tunneling Routes in Photosynthetic Reaction Center Alternate Due toThermal Fluctuation of Protein Conformation. *J. Phys. Chem. B* **2005**, *109*, 1978.

(21) Kawatsu, T.; Kakitani, T.; Yamato, T. Worm Model for Electron Tunneling in Proteins: Consolidation of the Pathway Model and the Dutton Plot. *J. Phys. Chem. B* **2001**, *105*, 4424.

(22) Nishioka, H.; Kakitani, T. Average Electron Tunneling Route of the Electron Transfer in Protein Media. *J. Phys. Chem. B* **2008**, *112*, 9948.

(23) Skourtis, S. S.; Beratan, D. N. *Adv. Chem. Phys.* **1999**, *106*, 377.

(24) Regan, J. J.; Onuchic, J. N. *Adv. Chem. Phys.* **1999**, *107*, 497.

(25) Stuchebrukhov, A. A. Long-distance electron tunneling in proteins. *Theor. Chem. Acc.* **2003**, *110*, 291.

(26) Jordan, K. D.; Paddon-Row, M. N. *J. Phys. Chem.* **1992**, *96*, 1188.

(27) Liang, C.; Newton, M. D. *J. Phys. Chem.* **1992**, *96*, 2855.

(28) Curtiss, L. A.; Naleway, C. A.; Miller, J. R. Theoretical Study of Long-Distance Electronic Coupling in $H_2C(CH_2)_{n-2}CH_2$ Chains, $n = 3 - 16$. *J. Phys. Chem.* **1993**, *97*, 4050.

(29) Hayashi, S.; Kato, S. *J. Phys. Chem. A* **1998**, *102*, 2878.

(30) Kawatsu, T.; Matsuda, K.; Hasegawa, J. *J. Phys. Chem. A* **2011**, *115*, 10814.

(31) Nishioka, H.; Ando, K. *Phys. Chem. Chem. Phys.* **2011**, *13*, 7043.

(32) Wallrapp, F.; Voityuk, A.; Guallar, V. *J. Chem. Theory Comput.* **2009**, *5*, 3312.

(33) Voityuk, A. A. *Chem. Phys. Lett.* **2010**, *495*, 131.

(34) Migliore, A.; Corni, S.; Di Felice, R.; Molinari, E. Water-Mediated Electron Transfer between Protein Redox Centers. *J. Phys. Chem. B* **2007**, *111*, 3774.

(35) Prytkova, T. R.; Kurnikov, I. V.; Beratan, D. N. Ab Initio Based Calculations of Electron-Transfer Rates in Metalloproteins. *J. Phys. Chem. B* **2005**, *109*, 1618.

(36) Prytkova, T. R.; Kurnikov, I. V.; Beratan, D. N. Coupling Coherence Distinguishes Structure Sensitivity in Protein Electron Transfer. *Science* **2007**, *315*, 622.

(37) Di Donato, M.; Peluso, A.; Villani, G. J. *J. Phys. Chem. B* **2004**, *108*, 3068.

(38) Kim, J.; Stuchebrukhov, A. *J. Phys. Chem. B* **2000**, *104*, 8606.

(39) Ito, H.; Nakatsuji, H. *J. Comput. Chem.* **2001**, *22*, 265.

(40) Kitaura, K.; Ikeo, E.; Asada, T.; Nakano, T.; Uebayasi, M. Fragment molecular orbital method: an approximate computational method for large molecules. *Chem. Phys. Lett.* **1999**, *313*, 701.

(41) Nakano, T.; Kaminuma, T.; Sato, T.; Fukuzawa, K.; Akiyama, Y.; Uebayasi, M.; Kitaura, K. *Chem. Phys. Lett.* **2002**, *351*, 475.

(42) Fedorov, D. G.; Kitaura, K. The importance of three-body terms in the fragment molecular orbital method. *J. Chem. Phys.* **2004**, *120*, 6832.

(43) Mochizuki, Y.; Yamashita, K.; Murase, T.; Nakano, T.; Fukuzawa, K.; Takematsu, K.; Watanabe, H.; Tanaka, S. Large scale FMO-MP2 calculations on a massively parallel-vector computer. *Chem. Phys. Lett* **2008**, *457*, 396.

(44) Ikegami, T.; Ishida, T.; Fedorov, D. G.; Kitaura, K.; Inadomi, Y.; Umeda, H.; Yokokawa, M.; Sekiguchi, S. Fragment Molecular Orbital Study of the Electronic Excitations in the Photosynthetic Reaction Center of Blastochloris viridis. *J. Comput. Chem.* **2010**, *31*, 447.

(45) Fletcher, G. D.; Fedorov, D. G.; Pruitt, S. R.; Windus, T. L.; Gordon, M. S. *J. Chem. Theory Comput.* **2012**, *8*, 75.

(46) Tsuneyuki, S.; Kobori, T.; Akagi, K.; Sodeyama, K.; Terakura, K.; Fukuyama, H. Molecular orbital calculation of biomolecules with fragment molecular orbitals. *Chem. Phys. Lett.* **2009**, *476*, 104.

(47) Nishioka, H.; Ando, K. Electronic coupling calculation and pathway analysis of electron transfer reaction using ab initio fragment-based method. I. FMO-LCMO approach. *J. Chem. Phys.* **2011**, *134*, 204109.

(48) Kurnikov, I. V.; Beratan, D. N. Ab initio based effective Hamiltonians for long-range electron transfer: Hartree-Fock analysis. *J. Chem. Phys.* **1996**, *105*, 9561.

(49) Balabin, I. A.; Onuchic, J. N. *Science* **2000**, *290*, 114.

(50) Plato, M.; Michel-Beyerle, M. E.; Bixon, M.; Jortner, J. On the role of tryptophan

as a superexchange mediator for quinone reduction in photosynthetic reaction centers. *FEBS Letters* **1989**, *249*, 70.

(51) Cave, R. J.; Newton, M. D. *Chem. Phys. Lett.* **1996**, *249*, 15.

(52) Cave, R. J.; Newton, M. D. Calculation of electronic coupling matrix elements for ground and excited state electron transfer reactions: Comparison of the generalized Mulliken-Hush and block diagonalization methods. *J. Chem. Phys.* **1997**, *106*, 9213.

(53) Voityuk, A. A.; Rösch, N. Fragment charge difference method for estimating donor-acceptor electronic coupling: Application to DNA π-stacks. *J. Chem. Phys.* **2002**, *117*, 5607.

(54) Kawatsu, T.; Kakitani, T.; Yamato, T. On the Anomaly of the Tunneling Matrix Element in Long-Range Electron Transfer. *J. Phys. Chem. B* **2002**, *106*, 5068.

(55) Debus, R. J.; Feher, G.; Okamura, M. Y. *Biochemistry* **1986**, *25*, 2276.

(56) Deisenhofer, J.; Epp, O.; Sinning, I.; Michel, H. *J. Mol. Biol.* **1995**, *246*, 429.

(57) Stewart, J. J. P. *J. Comput. Chem.* **1989**, *10*, 209.

(58) Frisch, M. J. *et al.*; Gaussian 09, revision B.01, Gaussian, Inc., Wallingford CT, **2010**.

(59) Feher, G.; Okamura, M. Y. *Appl. Magn. Reson.* **1999**, *16*, 63.

(60) Schmidt, M. W.; Baldridge, K. K.; Boatz, J. A.; Elbert, S. T.; Gordon, M. S.; Jensen, J. H.; Koseki, S.; Matsunaga, N.; Nguyen, K. A.; Su, S. J. et al. *J. Comput. Chem.* **1993**, *14*, 1347.

(61) Graige, M. S.; Feher, G.; Okamura, M. Y. *Proc. Natl. Acad. Sci. USA* **1998**, *95*, 11679.

(62) Li, J.; Takahashi, E.; Gunner, M. R. *Biochemistry* **2000**, *39*, 7445.

(63) Leibl, W.; Breton, J. *Biochemistry* **1991**, *30*, 9634.

(64) Mathis, P.; Sinning, I.; Michel, H. *Biochim. Biophys. Acta* **1992**, *1098*, 151.

(65) Kim, K.; Jordan, K. D.; Paddon-Row, M. N. *J. Phys. Chem.* **1994**, *98*, 11053.

(66) Yang, C.-H.; Hsu, C.-P. *J. Chem. Phys.* **2006**, *124*, 244507.

(67) Kirmaier, C.; Holten, D.; Debus, R. J.; Feher, G.; Okamura, M. Y. *Proc. Natl. Acad. Sci. USA* **1986**, *83*, 6407.

(68) Ishikita, H.; Knapp, E.-W. *FEBS Lett.* **2006**, *580*, 4567.

(69) Rabenstein, B.; Ullmann, G. M.; Knapp, E.-W. *Biochemistry* **1998**, *37*, 2488.

(70) Kleinfeld, D.; Okamura, M. Y.; Feher, G. *Biochemistry* **1984**, *23*, 5780.

(71) Utschig, L. M.; Thurnauer, M. C.; Tiede, D. M.; Poluektov, O. G. *Biochemistry* **2005**, *44*, 14131.

(72) Stowell, M. H. B.; McPhillips, T. M.; Rees, D. C.; Soltis, S. M.; Abresch, E.; Feher, G. *Science* **1997**, *276*, 812.

(73) Breton, J. *Biochemistry* **2004**, *43*, 3318.

(74) Xu, Q.; Baciou, L.; Sebban, P.; Gunner, M. R. *Biochemistry* **2002**, *41*, 10021.

(75) Baxter, R. H. G.; Ponomarenko, N.; Srajer, V.; Pahl, R.; Moffat, K.; Norris, J. R. *Proc. Natl. Acad. Sci. USA* **2004**, *101*, 5982.

(76) Li, J.; Gilroy, D.; Tiede, D. M.; Gunner, M. R. *Biochemistry* **1998**, *37*, 2818.

Table 1: Calculated electronic coupling T_{DA}, **ET rate** $k_{\mathrm{DA}}^{\mathrm{calc}}$, **and ET time** $1/k_{\mathrm{DA}}^{\mathrm{calc}}$ **at the 6-31G(d) level for the ET from** $\mathbf{H}_L$ **to MQ in the model system (A).**

Method		$\|T_{\mathrm{DA}}\|$ cm^{-1}	$k_{\mathrm{DA}}^{\mathrm{calc}}$ $\times 10^9\ \mathrm{s}^{-1}$	$1/k_{\mathrm{DA}}^{\mathrm{calc}}$ ps
RHF	GMH	3.46	3.22	310.
FMO-LCMO	GMH	3.85	3.96	252.
	bridge GF	3.26	2.85	351.
FMO-LCVMO	GMH	3.77	3.81	263.
	bridge GF	3.16	2.67	375.

Table 2: Calculated electronic coupling T_{DA}, ET rate $k_{\mathrm{DA}}^{\mathrm{calc}}$, and ET time $1/k_{\mathrm{DA}}^{\mathrm{calc}}$ at the 6-31G(d) level for the ET from MQ to UQ in the model systems (B) and (C). The $1/k_{\mathrm{DA}}^{\mathrm{obs}}$'s are taken from Refs 63,64. The numerical figures in parenthesis are $1/k_{\mathrm{DA}}^{\mathrm{obs}}$ for the ETs from $\mathrm{Q_A}$ to $\mathrm{Q_B}$ in the RCs of *Rba. sphaeroides* R-26.1.[55]

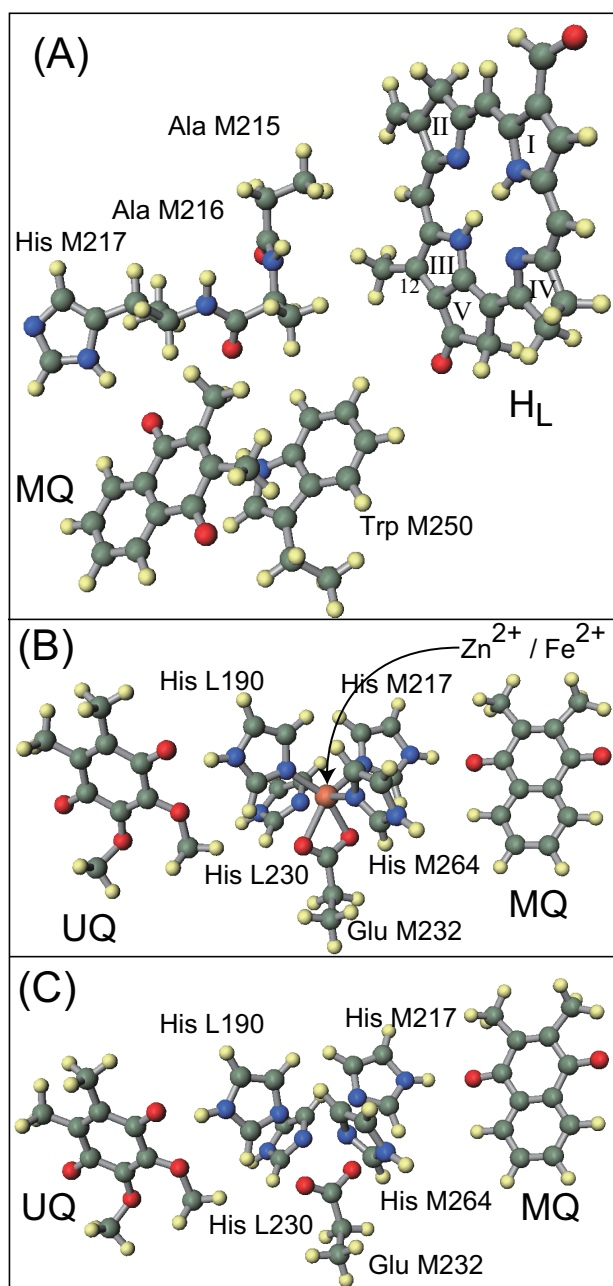| Metal ion	Method		$|T_{\mathrm{DA}}|$ $\mathrm{cm^{-1}}$	$k_{\mathrm{DA}}^{\mathrm{calc}}$ $\times 10^4\ \mathrm{s^{-1}}$	$1/k_{\mathrm{DA}}^{\mathrm{calc}}$ $\mu\mathrm{s}$	$1/k_{\mathrm{DA}}^{\mathrm{obs}}$ $\mu\mathrm{s}$
$\mathrm{Fe^{2+}}$(high-spin)	UHF	GMH	1.33	10.5	9.48	25 - 36
		bridge GF	1.39	11.5	8.68	(150)
$\mathrm{Fe^{2+}}$(low-spin)	RHF	GMH	0.944	5.35	18.7	
	FMO-LCMO	GMH	0.955	5.47	18.3	
		bridge GF	0.979	5.75	17.4	
	FMO-LCVMO	GMH	0.766	3.52	28.4	
		bridge GF	0.777	3.63	27.6	
$\mathrm{Zn^{2+}}$	RHF	GMH	1.30	10.1	9.93	(140)
	FMO-LCMO	GMH	1.31	10.4	9.65	
		bridge GF	1.34	10.9	9.21	
	FMO-LCVMO	GMH	1.20	8.68	11.5	
		bridge GF	1.23	9.02	11.1	
none	RHF	GMH	0.610	2.23	44.8	(350)
	FMO-LCMO	GMH	0.649	2.53	39.4	
		bridge GF	0.655	2.57	38.8	
	FMO-LCVMO	GMH	0.731	3.21	31.2	
		bridge GF	0.737	3.26	30.7	

Figure 1: Model systems for (A) the ET from H_L to MQ, (B)the ET from MQ to UQ involving the metal ion Fe^{2+} or Zn^{2+}, and (C) the ET from MQ to UQ not involving a metal ion.
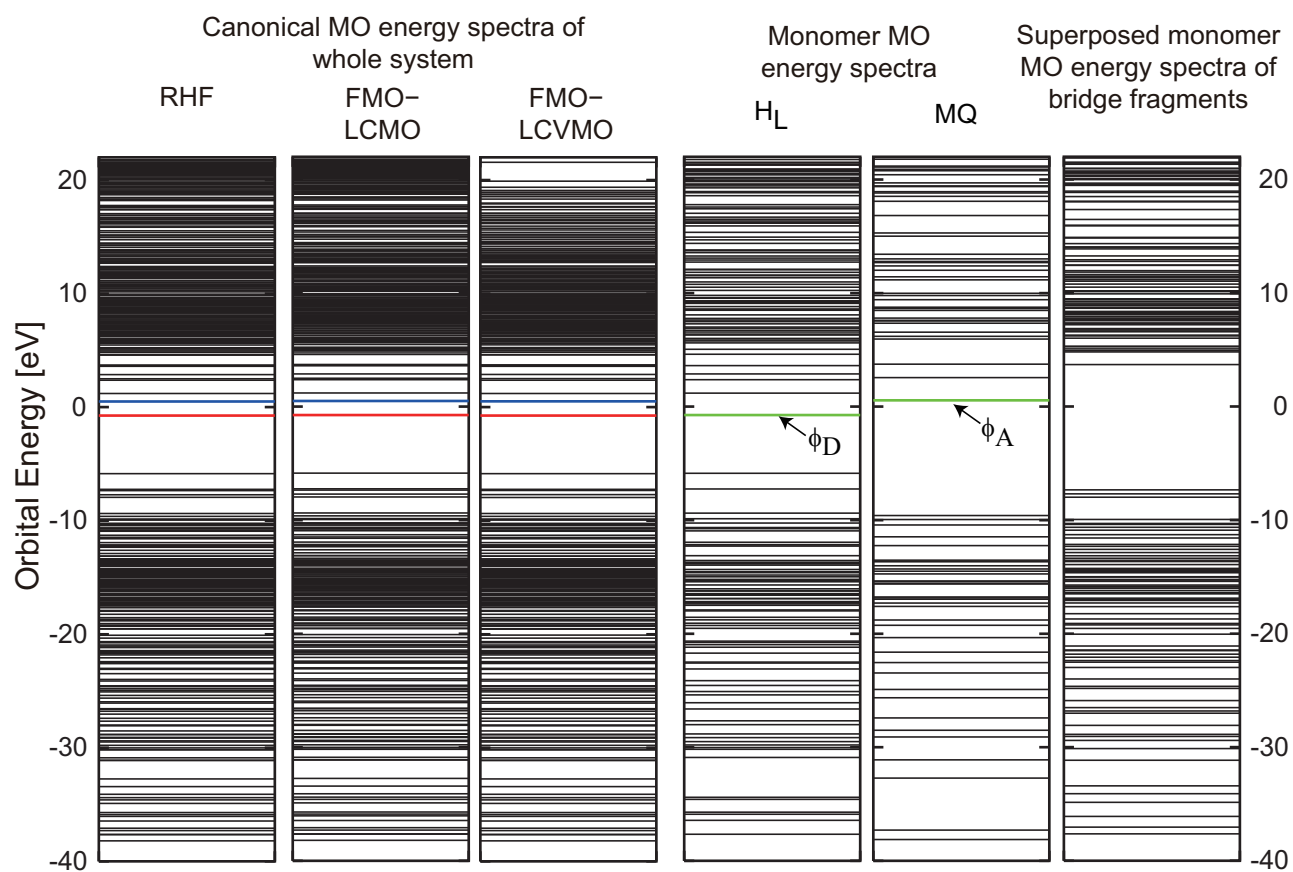
Figure 2: Canonical MO energy spectra obtained from the RHF, FMO-LCMO, and FMO-LCVMO methods with the 6-31G(d) basis set for the model system (A). Monomer MO energy spectra obtained from the FMO2 calculations for the H_L and MQ fragments and superposed spectrum of monomer MO energies obtained for each {Ala M215 + Ala M216 + His M217} and Trp M250 fragments are also plotted. The red and blue lines correspond to ψ_1 and ψ_2, respecitvely.
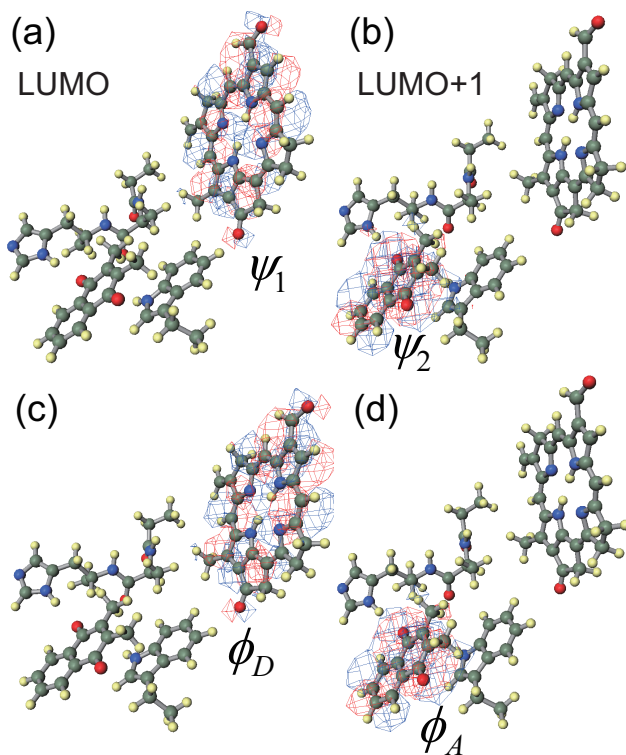
Figure 3: Frontier MOs obtained from RHF (a,b) and FMO2 (c,d) calculations for the model system (A) at the 6-31G(d) level. (a) LUMO, ψ_1, of the whole system. (b) LUMO+1, ψ_2, of the whole system. (c) LUMO of the H_L fragment used as the donor orbital ϕ_D. (d) LUMO of the MQ fragment used as the acceptor orbital ϕ_A. The isosurface values are ± 0.01. The atomic view and MOs are produced with use of Winmostar.
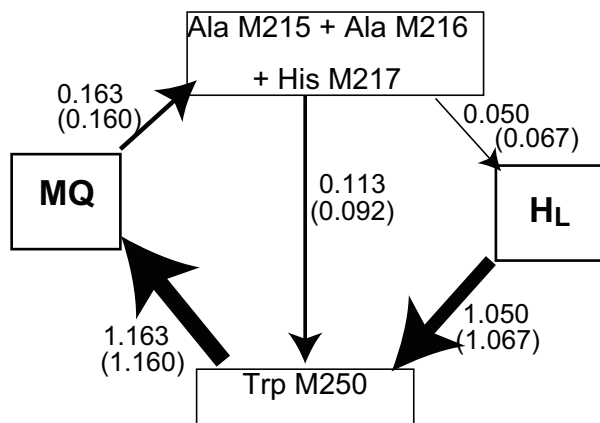
Figure 4: Map of normalized inter-fragment tunneling currents $K_{L,M}$ obtained for the model system (A) with the 6-31G(d) basis set. The arrows represent the $K_{L,M}$'s, with the thickness roughly proportional to their absolte values. The numerical figure near each arrow for its $|K_{L,M}|$ value from the FMO-LCMO calculation, and the figure in parentheses is the corresponding value from the FMO-LCVMO calculation
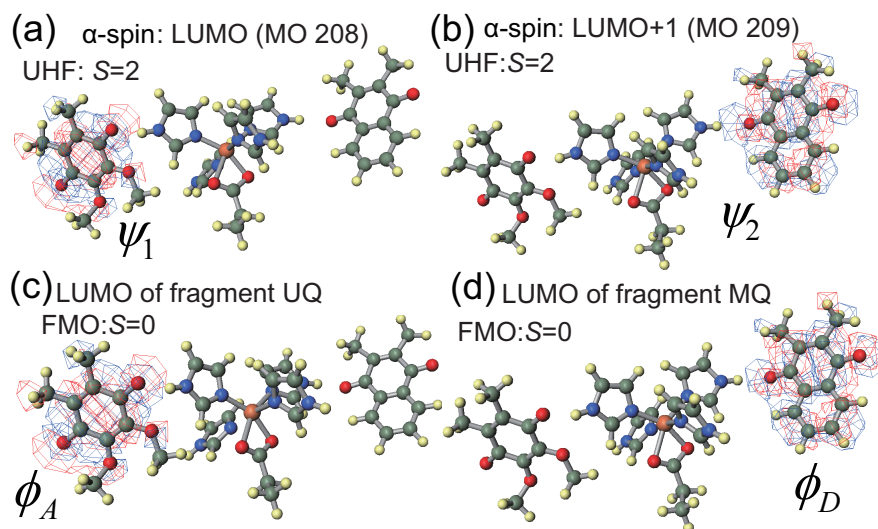
Figure 5: Frontier MOs calculated for the model system (B) with Fe^{2+} at the 6-31G(d) level. (a) α-spin LUMO and (b) LUMO+1 were obtained from UHF calculation for cation quintet state. (c) LUMO of the UQ fragment and (d) LUMO of the MQ fragment were obtained from FMO calculation for cation singlet state.
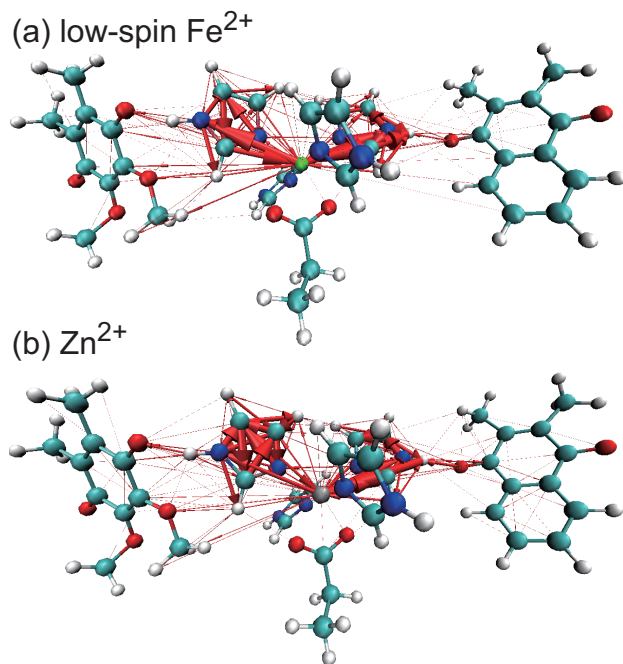

Figure 6: Map of normalized inter-atomic tunneling currents $K_{a,b}$ obtained for systems (B) with (a) low-spin Fe^{2+} and (b) Zn^{2+} at the 6-31G(d) level. The $K_{a,b}$ is represented by the arrow with width proportional to its amplitude. The atomic view is produced with use of VMD.
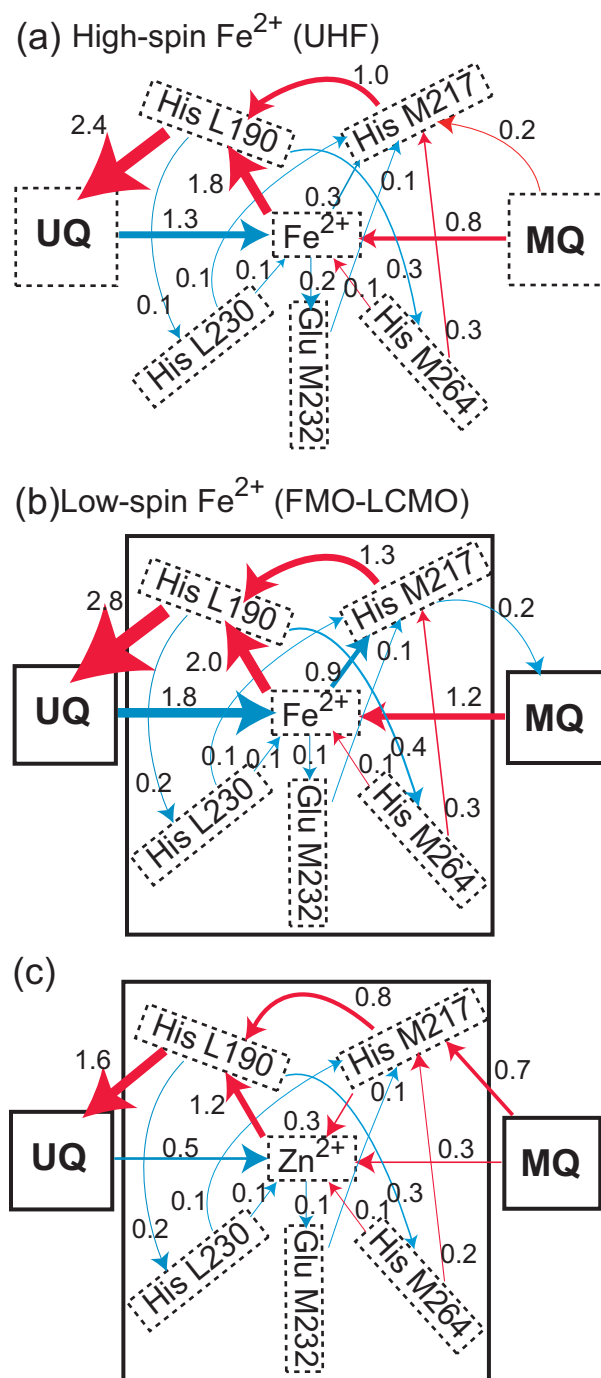
Figure 7: Maps of $K_{\mathrm{Res}X,\mathrm{Res}Y}$ obtained for systems (B) with (a) high-spin Fe^{2+}, (b) low-spin Fe^{2+}, and (c) Zn^{2+}. The solid square represents the fragment used in the FMO2 calculations. The dashed square represents the Res X. Notation is the same as in Figure 4. The 6-31G(d) basis set was used.
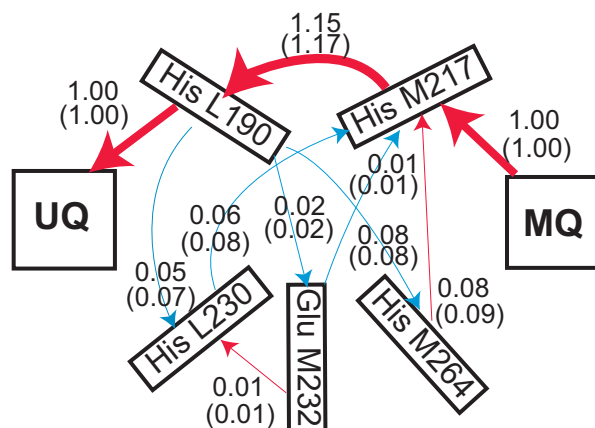
Figure 8: Map of $K_{L,M}$ obtained for system (C). Notation is the same as in 4. The 6-31G(d) basis set was used.
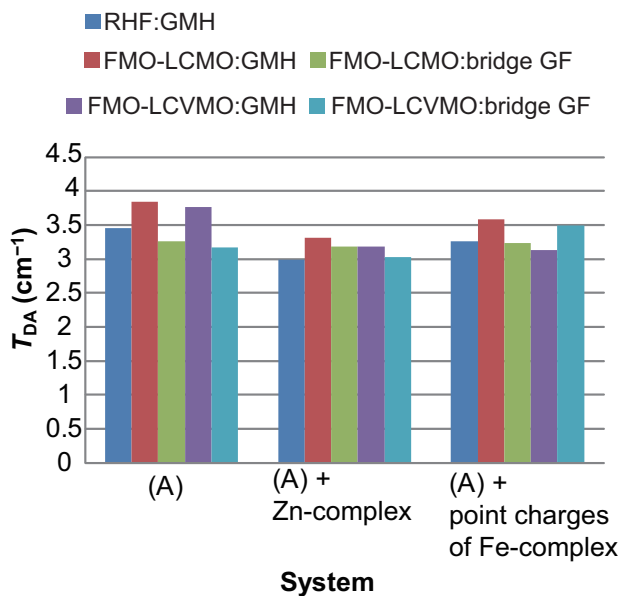

Figure 9: Electronic couplings, T_{DA}'s, obtained for systems (A) + Zn-complex and (A) + point charges of Fe-complex. T_{DA}'s for system (A) are listed in Table 1. The 6-31G(d) basis set was used.

Graphical TOC Entry